Supplemental Document

Optics Letters

Compressed ultrafast tomographic imaging by passive spatiotemporal projections: supplement

YINGMING LAI,[1] RUIBO SHANG,[2] CHRISTIAN-YVES CÔTÉ,[3] XIANGLEI LIU,[1] ANTOINE LARAMÉE,[1] FRANÇOIS LÉGARÉ,[1] GEOFFREY P. LUKE,[2] AND JINYANG LIANG[1,*]

[1] *Centre Énergie Matériaux Télécommunications, Institut National de la Recherche Scientifique, 1650 Boulevard Lionel-Boulet, Varennes, Québec J3X1S2, Canada*
[2] *Thayer School of Engineering, Dartmouth College, 14 Engineering Drive, Hanover, New Hampshire 03755, USA*
[3] *Axis Photonique Inc., 1650 Boulevard Lionel-Boulet, Varennes, Québec J3X1S2, Canada*
[*] *Corresponding author: jinyang.liang@emt.inrs.ca*

Supplement DOI: https://doi.org/10.6084/m9.figshare.14180045

Parent Article DOI: https://doi.org/10.1364/OL.420737

Compressed Ultrafast Tomographic Imaging by Passive Spatiotemporal Projections: supplemental document

1. Comparison between CUTI and CUP

Despite both being ultrafast imaging methods, compressed ultrafast tomographic imaging (CUTI) is conceptually different from compressed ultrafast photography (CUP) (summarized in Table S1). CUTI, by grafting the principle of sparse-view computed tomography (CT) [1] to the spatiotemporal domain, is a multiple-shot ultrafast imaging method but does not require any spatial encoding. CUP, on the contrary, is built upon single-shot coded-aperture imaging [2]. It uses compressed sensing (CS) and streak imaging to capture transient events with single camera exposure, which requires a random binary mask to spatially encode the input scenes [3, 4].

The principle of CUTI has been explained in detail in Main Text. The forward and backward models are written as Eqs. (1) and (2). The principle of CUP is different from CUTI. In data acquisition, a dynamic event $I(x, y, t)$ is first spatially encoded by a random binary mask. This process is denoted by the spatial encoding operator $\boldsymbol{C}$. Then, the encoded scene is sheared along one spatial direction, which is denoted by the temporal shearing operator $\boldsymbol{S}$. Finally, the spatially encoded, temporally sheared scene is recorded by a camera, which is denoted by the spatiotemporal integration operator $\boldsymbol{T}$. Overall, the forward model of CUP can be described as

$$E = \boldsymbol{TSC}\, I(x, y, t). \tag{S1}$$

In CUP's image reconstruction, $I(x, y, t)$ is recovered by solving the minimization problem of

$$\hat{I} = \arg\min_{I} \left\{ \frac{1}{2} \| E - \boldsymbol{TSC} I \|_2^2 + \tau \Phi_{\mathrm{TV}}(I) \right\}, \tag{S2}$$

where τ is the regularization parameter, and Φ_{TV} is the total-variation (TV) regularization function.

Table S1. Comparison of operating principles between CUP and CUTI

Image modality		CUP [3]	CUTI
Required number of measurements		Single-shot	Multiple-shot $E = [E_1, E_2, \dots, E_N]^T$
Theoretical foundation		Single-shot coded-aperture imaging	Sparse-view computed tomography
Forward model	Spatial encoding	Yes	No
	Temporal shearing	Single sweep	Multiple sweeps with different shearing velocities $\boldsymbol{S} = [\boldsymbol{S}_1, \boldsymbol{S}_2, \dots, \boldsymbol{S}_N]^{\boldsymbol{T}}$
	Spatiotemporal integration	Yes	Yes
	Formula	$E = \boldsymbol{TSC}\, I(x, y, t)$	$E = \boldsymbol{TS}\, I(x, y, t)$
Backward model	Formula	$\hat{I} = \arg\min_{I} \left\{ \frac{1}{2} \| E - \boldsymbol{TSC} I \|_2^2 + \tau \Phi_{\mathrm{TV}}(I) \right\}$	$\hat{I} = \arg\min_{I} \left\{ \frac{1}{2} \| E - \boldsymbol{TS} I \|_2^2 + \tau \Phi_{\mathrm{TV}}(I) \right\}$

Note: N is the total number of measurements.

2. Simulation of CUTI and multi-encoding CUP

Multi-encoding (ME)-CUP, different from most CUP techniques, has been demonstrated as a multiple-shot ultrafast imaging technique [5]. In each data acquisition, a dynamic event $I(x, y, t)$ is spatially encoded by a different mask, denoted by $\boldsymbol{C}_{\mathrm{ME}_i}(x, y)$, where $i = 1, 2, \ldots, N$. Then, the encoded scenes are sheared along one spatial direction at the same shearing velocity. Finally, a CCD camera records these spatially encoded, temporally sheared scenes using spatiotemporal integration. Overall, the forward model of multi-shot ME-CUP is

$$E_{\mathrm{ME}} = \boldsymbol{TSC}_{\mathrm{ME}}\, I(x, y, t), \quad \text{(S3)}$$

where $E_{\mathrm{ME}} = \left[E_{\mathrm{ME}_1}, E_{\mathrm{ME}_2}, \ldots, E_{\mathrm{ME}_N}\right]^T$ and $\boldsymbol{C}_{\mathrm{ME}} = \left[\boldsymbol{C}_{\mathrm{ME}_1}, \boldsymbol{C}_{\mathrm{ME}_2}, \ldots, \boldsymbol{C}_{\mathrm{ME}_N}\right]^T$. In image reconstruction, $I(x, y, t)$ is recovered by solving the minimization problem

$$\hat{I} = \arg\min_{I}\left\{\frac{1}{2}\|E_{\mathrm{ME}} - \boldsymbol{TSC}_{\mathrm{ME}} I\|_2^2 + \tau\Phi_{\mathrm{TV}}(I)\right\}. \quad \text{(S4)}$$

To better compare multi-shot ME-CUP and CUTI, we simulated the performance of these two methods by a dynamic jellyfish scene with the size of $N_x \times N_y \times N_t = 512 \times 512 \times 80$ pixels. To make a fair comparison to the simulation conditions used to CUTI, we set $N = 5$ for ME-CUP. The encoding pixels in the five random binary masks have 2×2 pixels in size. The datacube is inputted into Eq. (S3) to generate a simulated streak image set E_{ME}. Then, the datacube is recovered from the streak images by the TwIST algorithm [6] with $\tau = 2 \times 10^{-8}$.

The full evolution is shown in Visualization S1. Fig. S1(a) shows four selected frames and a zoomed-in view of a local region from the ground truth (GT), the reconstruction of ME-CUP, and the reconstruction of CUTI. Fig. S1(b) shows three features in the zoom-in view of the GT and the reconstructions. The result shows that ME-CUP's reconstruction blurs these features. In contrast, CUTI can accurately preserve the sharpness of these features. Therefore, without the need for spatial encoding, CUTI offers a higher reconstruction accuracy. It also makes CUTI adaptable to existing streak cameras without any hardware modification.

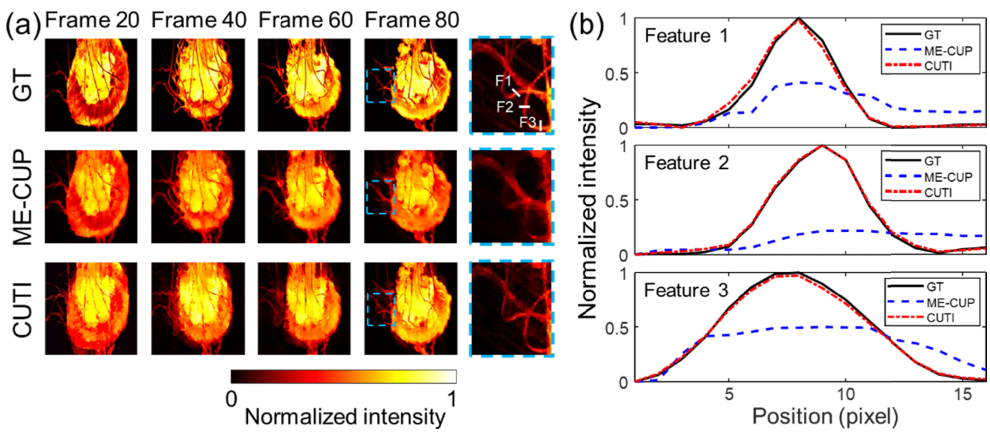

Fig. S1. Comparison of the ground truth (GT) with the reconstruction of multiple-shot ME-CUP and CUTI. (a) Four representative frames of the GT, ME-CUP, and CUTI. Last column: zoomed-in views of a local region in the 80th frame (marked by the cyan dashed box). (b) Line profiles of the three selected features in the GT [marked as F1–F3 the last panel of the first row in Fig. S1(a)] and in the reconstructions of ME-CUP and CUTI.

3. Derivation of spatiotemporal projection angles in CUTI's data acquisition

In CUTI's data acquisition, the information in the y-axis and the t-axis are coupled in the temporal shearing operation. Then, the information is recorded in each discrete pixel on the streak camera's sensor by the spatiotemporal integration operation. Thus, the size of discrete pixels (denoted by p_c) and the maximum shearing velocity (denoted by $\boldsymbol{v}_{\max}$) determine the maximum resolving capability of CUTI in the t-axis. CUTI's imaging speed, r, is calculated by

$$r = \frac{|\boldsymbol{v}_{\max}|}{p_{\mathrm{c}}}. \tag{S5}$$

In addition, the observation time window is determined by the sweep time, denoted by t_{s}. Therefore, CUTI's sequence depth is calculated by

$$N_t = rt_{\mathrm{s}}. \tag{S6}$$

As illustrated in Fig. 1 in Main text, the operations of temporal shearing and spatiotemporal integration are equivalent to a passive projection in the y-t plane. At the shearing velocity in the i^{th} acquisition (denoted by $\boldsymbol{v}_i$), the total shearing distance, in terms of the number of pixels, is expressed by

$$N_{\mathrm{s}} = \frac{\boldsymbol{v}_i t_{\mathrm{s}}}{p_{\mathrm{c}}}. \tag{S7}$$

Thus, the projection angle in the i^{th} acquisition, denoted by θ_i, is determined by

$$\theta_i = \tan^{-1}\left(\frac{N_{\mathrm{s}}}{N_t}\right) = \tan^{-1}\left(\frac{\boldsymbol{v}_i}{|\boldsymbol{v}_{\max}|}\right). \tag{S8}$$

Because the temporal shearing operation can be performed in both directions along the y-axis, $\boldsymbol{v}_i \in [-|\boldsymbol{v}_{\max}|, +|\boldsymbol{v}_{\max}|]$. Therefore, the angle of spatiotemporal projection $\theta_i \in [-45°, +45°]$.

4. Compensation for aberrations in the image-converter streak camera

Three sources contribute to the aberrations in the image-converter streak camera. Each aberration is carefully compensated for in the experiment. The first source of aberration comes from the trajectory length difference of photoelectrons. This aberration is calibrated by the curvature correction conducted during the initial test of this streak camera. The second distortion comes from the defocusing of photoelectrons deflected to the lower part of the streak images. This aberration is partially rectified by curvature correction and by limiting the sweep time. However, limited by the design of the streak tube, the residue of uncorrected aberration persists in the captured projection images, which contributes to the decrease of the image quality. The last source of aberration comes from the space-charge effect of photoelectrons at the focus of the electron imaging system in the streak tube. This aberration is minimized by balancing the incident laser pulse energy and the signal gain in the streak camera. In contrast, the rotating-mirror streak camera operates all-optically. Its design also satisfies the paraxial approximation. Thus, these sources of aberration do not exist, which results in better quality in the acquired projection images.

It is worth noting that CUTI's operation does not rely on the full elimination of the aberrations, as demonstrated from our experimental results presented in Figs. 3 and 4 in Main Text. Aberrations in the recorded projection images, nevertheless, can decrease both the spatial resolution and the temporal resolution. This effect has been illustrated in Fig. 3 in Main Text and discussed in the associated text.

References

1. H. Kudo, T. Suzuki, and E. A. Rashed, Quant. Imaging Med. Surg. **3**, 147 (2013).
2. J. Liang, Rep. Prog. Phys. **83**, 116101 (2020).
3. L. Gao, J. Liang, C. Li, and L. V. Wang, Nature **516**, 74 (2014).
4. S. Jalali and X. Yuan, IEEE Trans. Inf. Theory, **65**, 8005 (2019).
5. C. Yang, D. Qi, J. Liang, X. Wang, F. Cao, Y. He, X. Ouyang, B. Zhu, W. Wen, T. Jia, J. Tian, L. Gao, Z. Sun, S. Zhang, and L. V. Wang, Laser Phys. Lett. **15**, 116202 (2018).
6. J. M. Bioucas-Dias and M. A. T. Figueiredo, IEEE Trans. Image Process. **16**, 2992 (2007).